Available online at www.sciencedirect.com
ScienceDirect
Trans. Nonferrous Met. Soc. China 35(2025) 77−90
Transactions of Nonferrous Metals Society of China
www.tnmsc.cn

In-situ Si particle-reinforced joints of hypereutectic Al−60Si alloys by ultrasonic-assisted soldering

Yuan-xing LI, Xiang-bo ZHENG, Chao-zheng ZHAO, Zong-tao ZHU, Yu-jie BAI, Hui CHEN

Key Laboratory of Advanced Technologies of Materials, Ministry of Education,
School of Materials Science and Engineering, Southwest Jiaotong University, Chengdu 610031, China

Received 13 June 2023; accepted 22 November 2023

Abstract: To improve the wettability of hypereutectic Al−60Si alloy and enhance the mechanical properties of the joints, Al−60Si alloy was joined by ultrasonic soldering with Sn–9Zn solder, and a sound joint with in-situ Si particle reinforcement was obtained. The oxide film of Al−60Si alloy at the interface was identified by transmission electron microscopy (TEM) analysis as amorphous Al_2O_3. The oxide of Si particles in the base metal was also alumina. The oxide film of Al−60Si alloy was observed to be removed by ultrasonic vibration instead of holding treatment. Si particle-reinforced joints (35.7 vol.%) were obtained by increasing the ultrasonication time. The maximum shear strength peaked at 99.5 MPa for soldering at 330 °C with an ultrasonic vibration time of 50 s. A model of forming of Si particles reinforced joint under the ultrasound was proposed, and ultrasonic vibration was considered to promote the dissolution of Al and migration of Si particles.

Key words: hypereutectic Al−60Si alloy; ultrasonic-assisted soldering; Si particle reinforcement; Sn−9Zn solder

1 Introduction

Hypereutectic Al–Si alloys with high Si content have numerous advantages, including high specific strength [1−3], low adjustable thermal expansion [4], high thermal conductivity [5], and good wear resistance and corrosion properties [6,7]. In addition, hypereutectic Al−Si alloys have good plating ability and laser weldability, which allow them to be widely applied in many fields, such as electronic packaging, automotive industry, and machinery [8]. However, compared with conventional metals and alloys, Al–high-Si alloys exhibit relatively poor machinability. Therefore, welding methods are often required to expand the range of application of these hypereutectic Al−Si alloys [9].

Owing to the large difference in physical and chemical properties of silicon particles and the base aluminum alloy, it is difficult to obtain a sound joint involving hypereutectic Al−Si alloys. The joining methods for these alloys include fusion welding [10], friction stir welding [11], transient liquid-phase (TLP) bonding [12], and ultrasonic brazing [13−15]. However, fusion welding methods are associated with high heat output, which decreases mechanical properties of the joints. For instance, fine Si particles can grow into coarse Si phases at elevated temperature using TIG and CO_2 laser welding, which reduce the mechanical properties of the joints of Al−high-Si alloys [10,16]. These processes are also not suitable for large-area welding of hypereutectic Al–Si alloys in electronic applications. High-strength joints with fine Si particles are achieved by friction stir welding [17]; however, this technique is not suitable for welding an irregular seam of a packaging box. Therefore,

Corresponding author: Yuan-xing LI, Tel: +86-28-87600722, E-mail: yxlc8112@163.com
https://doi.org/10.1016/S1003-6326(24)66666-5

low-temperature welding techniques with process flexibility should be considered to join hypereutectic Al−Si alloys.

However, oxide films of hypereutectic Al−Si alloys were hardly to remove by the low-temperature welding methods. Hypereutectic Al−Si alloys were recently successfully welded by partial TLP (transient liquid phase) bonding and ultrasonic-assisted bonding [18,19]. SUN et al [20] successfully bonded Al−27Si and Al−50Si alloys by partial TLP bonding at 530 °C in vacuum, yielding a strong metallurgical joint using a Cu interlayer. XU et al [21] obtained a high-strength bond of an Al/Al−27Si joint using partial TLP bonding at 550 °C. Ultrasonic cavitation has successfully been utilized to remove the oxide film and enhance wettability [22,23]. Ultrasonic-assisted brazing and soldering are suitable for welding aluminum matrix composites [24]. A Zn-based interlayer was used to achieve a sound joint of Al−50Si alloy at a lower temperature (390 °C) by ultrasound-induced TLP bonding [25]. All the joints obtained were at a high temperature, which were not suitable for the joining of electronic packaging. ZHU et al [26] used Sn−5In filler metal to solder hypereutectic Al−Si alloys via an ultrasound-induced liquid-phase method at the relatively low temperature of 180 °C in air, and Si particles were induced into the bond; however, the joint strength was below 7 MPa.

The study showed that it is difficult to achieve a sound joint of hypereutectic Al−Si alloys at low temperature, which is required in the electronic packaging industry. In addition, the oxide film on the surface of high-Si aluminum alloys is considered a barrier to obtain a metallurgical bond. However, the microstructure of the oxide film and its removal from hypereutectic Al−Si alloys with a high content of Si particles on the surface is not clear. Therefore, the removal behavior of oxide film of hypereutectic Al−Si alloys were investigated through TEM observation. And Si particles were introduced in-situ into the weld to strengthen the joints of Al−60Si hypereutectic alloys by ultrasonic vibration with Sn−9Zn filler metal at low temperature. The microstructure evolution and mechanical properties of the joints, and the microstructure and removal of the oxide film under ultrasonic vibration were investigated in the present work.

2 Experimental

The experimental material was commercial hypereutectic Al−60wt.%Si alloy fabricated by hot pressing sintering method (Baienwei New Materials Technology Co., Ltd., Tianjin, China). The microstructure of hypereutectic Al−60Si alloy is shown in Fig. 1, where light grey phases and dark grey phases were identified as Si particles and Al substrate, respectively. And a small amount of impurity phases containing iron were also been found, as shown in Table 1. The thermal physical properties and mechanical properties of base Al−60Si alloys and Sn−9Zn solders are given in Table 2. Wetting experiments were carried out with specimens of 25 mm × 25 mm × 2 mm to investigate the removal of oxide. The filler metal mass was 0.4 g. Soldering experiments were carried out using samples of 50 mm × 10 mm × 3 mm, and the lap length is 10−15 mm. The hypereutectic Al−60Si samples were mechanically finished using abrasive paper from 300# to 2000# grit, and then ultrasonically cleaned in acetone for 30 min before joining. Self-made Sn−9wt.%Zn eutectic filler metal was used. The melting point of the Sn−9Zn alloy was 198 °C.

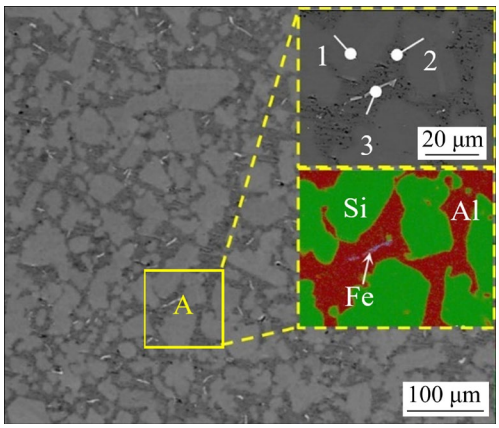

Fig. 1 Microstructure of hypereutectic Al−60Si alloy

Table 1 Compositions of phases in hypereutectic Al−60Si alloy in Fig. 1 (wt.%)

Point	Si	Al	Fe	Mn
1	99.74	0.26	−	−
2	−	100	−	−
3	10.94	65.93	22.67	0.46

Table 2 Thermal physical properties and mechanical properties of Al−60Si alloy and Sn−9Zn solders

Alloy	Thermal conductivity/ ($W \cdot m^{-2} \cdot K^{-1}$)	CTE/ K^{-1}	Tensile strength/MPa
Al−60Si	150	10.6×10^{-6}	181
Sn−9Zn	68.2	23.4×10^{-6}	38

Ultrasonic vibration with a power of 400 W, a pressure of 0.15 MPa, and an amplitude of 10 μm at a frequency of 20 kHz was applied on the lower Al−60Si alloy plate in the soldering experiments under atmospheric conditions, as shown in Fig. 2(a). The wetting experimental setup is shown in Fig. 2(b). The effect of soldering temperature was investigated in the range 240−360 °C and the ultrasonication time was 10 s. Samples were soldered with ultrasonic vibration for 10, 30, 50, 70, and 90 s to investigate the effect of ultrasonication time on the microstructure and mechanical properties of the joints.

Microstructures of the joints, including fracture surfaces, were investigated using field-emission scanning electron microscopy (SEM; FEI, Quanta FEG250, USA) combined with energy-dispersive X-ray spectroscopy (EDS) and transmission electron microscopy (TEM; FEI TECNAI G2 F20 X-Twin, USA). TEM accompanied by scanning transmission electron microscopy (STEM) and high-angle annular dark field (HADDF) analysis was used to investigate element distribution. The TEM samples were prepared using a focused ion beam (FIB; FEI-FIB Strata 400S, USA). Three parallel samples of the joints were tested for shear strength using an electronic tensile testing machine (Instron-5928, UK) with a pressure-head speed of 1 mm/min.

3 Results and discussion

3.1 Removal of oxide film

The removal behavior of oxide film of hypereutectic Al−60Si alloys is investigated through wetting experiment. Figure 3 shows interfaces between Sn−9Zn filler metal and Al−60Si alloy produced with different ultrasonic vibration time at 300 °C. At the start (ultrasonication time of 0.1 s), few areas of the oxide film were removed by ultrasonic cavitation and the Sn−9Zn solder spread on the Al−60Si surface with the most oxide film remaining (Fig. 3(a)). Figure 3(b) shows mapping of the element distribution. Si particles could be clearly seen in the Al matrix of the Al−60Si base metal. As the ultrasonic vibration time increased to 0.5 s, the remaining oxide film was observed as a black straight line in Figs. 3(c, d). Large amounts of aluminum dissolved into the seam, leaving the Si particles under the remaining oxide film. The maximum dissolution width of aluminum was about 14 μm. Figure 3(e) shows that the oxide film of the Al−60Si alloy was completely removed at an ultrasonic vibration time of 1 s and the maximum dissolution width of the aluminum increased to 22 μm. A dark red phase of aluminum dendrites could be seen in the seam (Fig. 3(f)). As the ultrasonic vibration time increased to 2 s, the

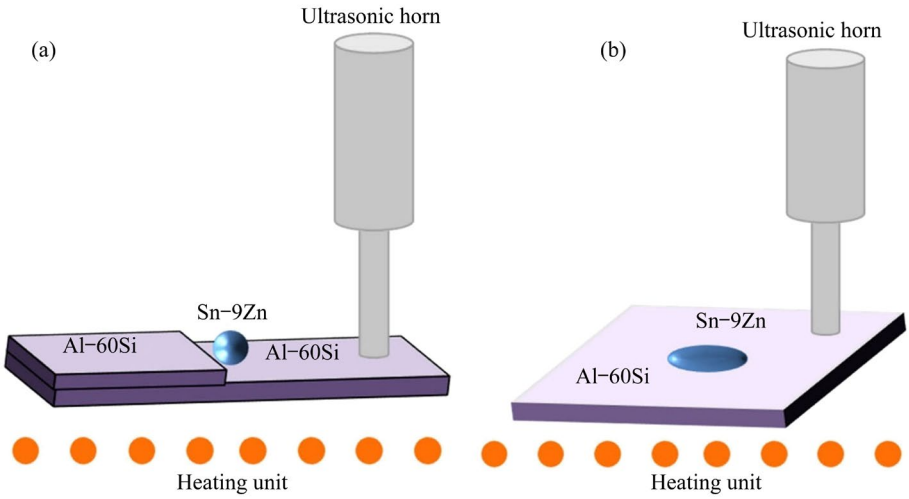

Fig. 2 Schematic diagrams of ultrasonic-assisted soldering (a) and wetting (b)

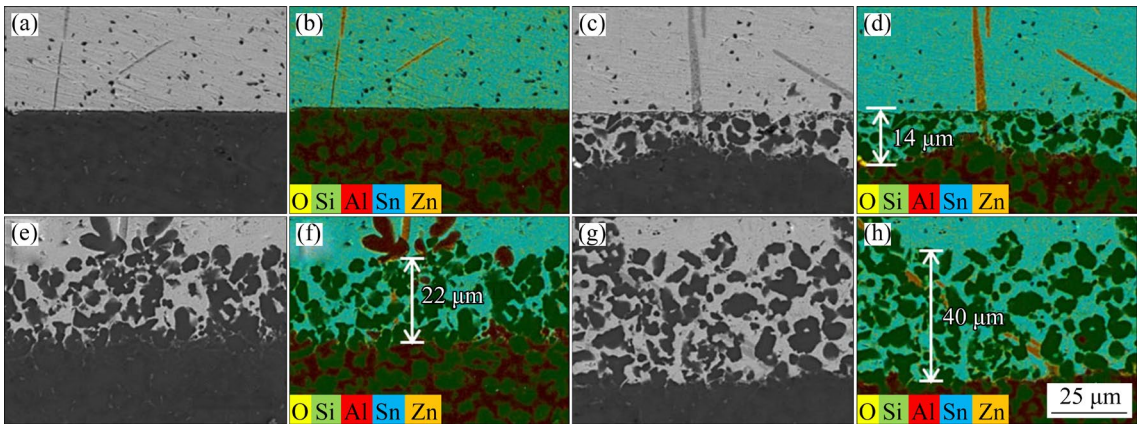

Fig. 3 Microstructure of interface (a, c, e, g) and mapping of element distributions (b, d, f, h) of Sn−9Zn/Al−60Si alloy soldered at 300 °C for different time: (a, b) 0.1 s; (c, d) 0.5 s; (e, f) 1 s; (g, h) 2 s

dissolution width increased to 40 μm (Fig. 3(h)). With increasing dissolution of Al, some Si particles without a surrounding Al matrix migrated into the seam under the ultrasonic vibration (Fig. 3(g)). Similar results were reported for the ultrasonic-assisted brazing of cemented carbide, in which WC particles were found to migrate into the seam due to dissolution of Co and the ultrasonic effect [27].

The magnified graph of the oxide film of the joints ultrasonic soldered for 0.5 s at 300 °C is shown in Fig. 4. The compositions of the residual oxide film and the phases identified by EDS analysis are given in Table 3. The composition test was not so exactly for the oxide film is too thin. However, the compositions of Points 1 and 2 containing plenty of oxygen element, and the line scanning results also show enrichment of oxygen element at the interface, as shown in Fig. 4(b).

Ultrasonic vibration is considered to remove the oxide film by the ultrasonic cavitation effect [23]. Although Fig. 3 suggests that the time for which the ultrasonic vibration was applied on the Al–60Si plates played an important role in removal of the oxide film, the mechanism by which the holding treatment affects the oxide removal is not clear. To investigate the effect of holding time on removal of the oxide film, the samples were held for different time after 0.1 s ultrasonic vibration, as shown in Fig. 5. Compared with Fig. 3(a), the most significant differences were the increase in the width of the Al dissolution (20 μm) for a holding time of 10 min and the appearance of obviously damaged oxide films at the interface. The dissolution width increased to 30 and 40 μm with

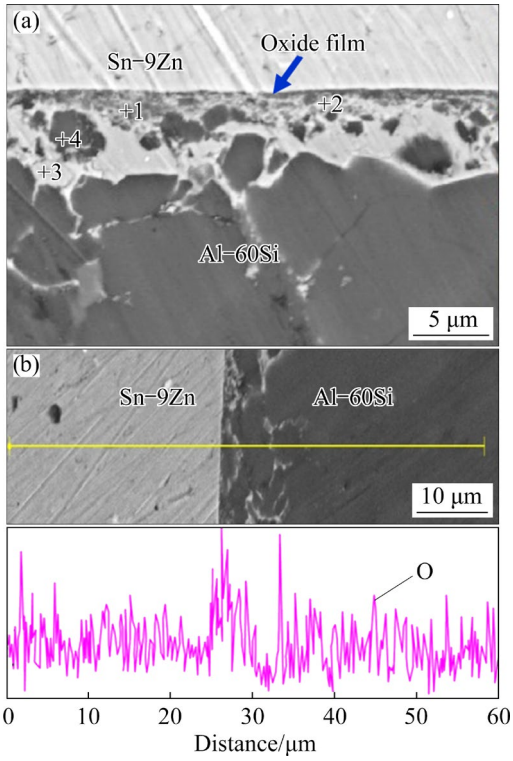

Fig. 4 Microstructure of oxide film (a) and line scanning of interface (b) of joints ultrasonically soldered for 0.5 s at 300 °C

Table 3 Compositions of oxide film and phases at interface in Fig. 4 (wt.%)

Point	Sn	Si	Al	Zn	O
1	58.48	3.32	26.31	0.9	10.99
2	58.15	6.07	20.11	0.6	15.07
3	87.13	0.53	10.36	0.89	1.09
4	19.12	75.64	2.32	0.3	2.62

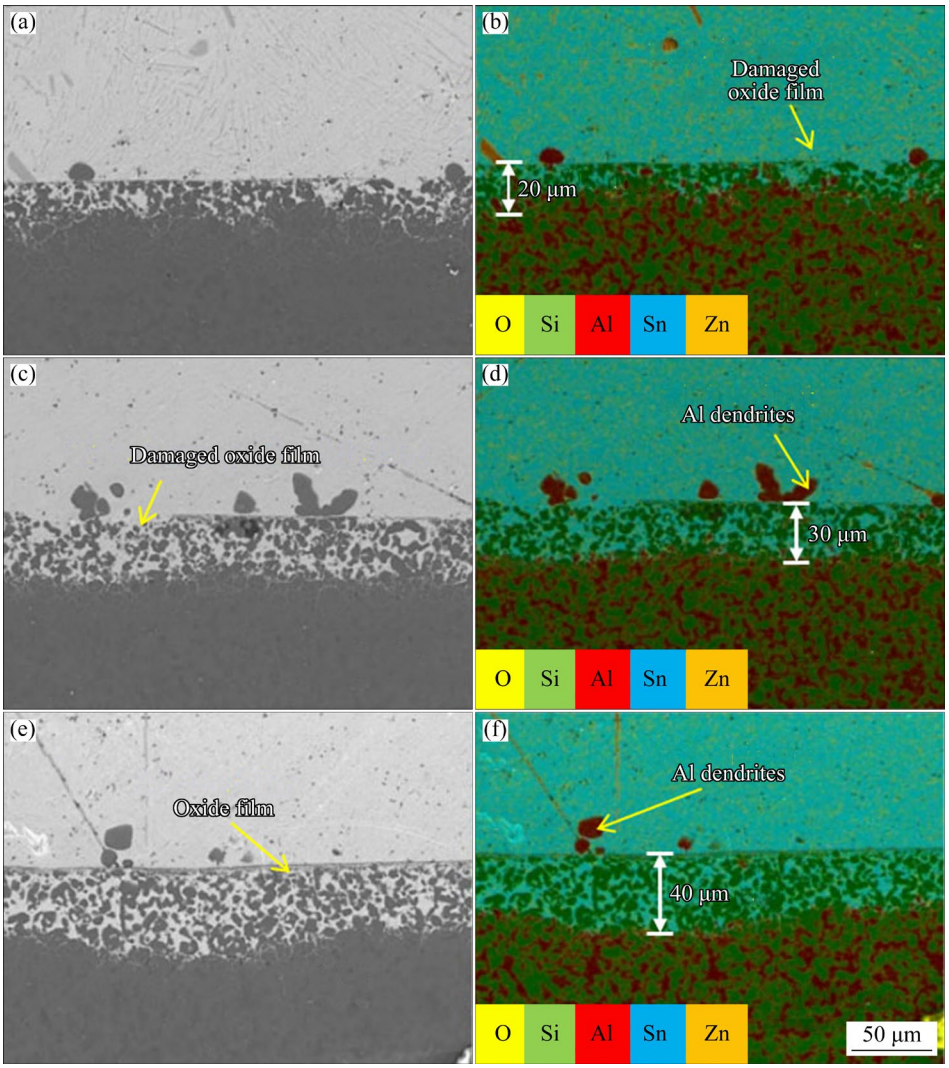

Fig. 5 Microstructures of interface (a, c, e) and mappings of element distribution (b, d, f) of Sn−9Zn/Al−60Si alloy soldered 300 °C for holding time: (a, b) 10 min; (b, c) 20 min; (e, f) 30 min

increasing holding time of 20 and 30 min, respectively, as shown in Figs. 5(c−f). This result implies that dissolution increased with holding time. Al dendrites were found in the seam (Figs. 5(d, f)); however, oxide film still remained between the Sn−9Zn filler and Al−60Si base metal. This suggests that the holding treatment could not remove the oxide film: holding time caused more base metal to dissolve into the solder; the oxide film was mainly removed by ultrasonic vibration.

The microstructure of the interface between Sn−9Zn solder and the Al−60Si alloy soldered at 300 °C with 0.1 s ultrasonic vibration was observed by TEM, as shown in Fig. 6. Figures 6(b−d) show the patterns of the marked regions in Fig. 6(a). Regions I and III were confirmed as Si particles and Sn−9Zn solder, respectively. Region II, the interface between Sn-based filler metal and Si particles, was identified as an amorphous layer.

The magnification of interface of Region II in Fig. 6 was observed using HADDF mode. The element distribution at the interface was studied by mapping scanning using the HADDF mode, as shown in Figs. 7(a−f). Figures 7(b, c) show that aluminum and oxygen were enriched at the interface, but no other elements were observed, implying that an aluminum oxide film existed in the interface. The oxide film of Al−60Si alloys was about 30−40 nm in width (Fig. 7(a)). The composition of the oxide film (Region A) is shown in Table 4, which confirmed an Al_2O_3 film by EDS results ($Al_{39.11}O_{60.42}Si_{0.26}Sn_{0.21}$). Figures 7(d−f) show that one side of the oxide film was composed of silicon particles, while the other side showed the presence of

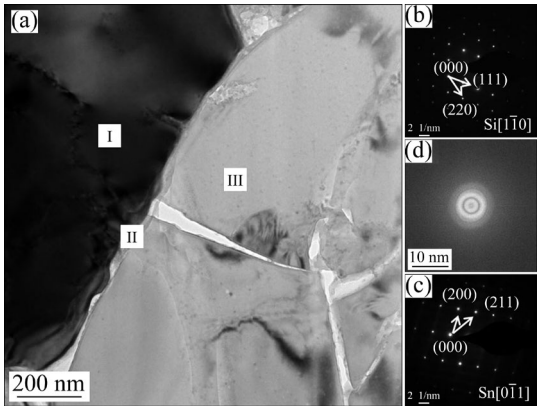

Fig. 6 Typical transmission electron micrographs of interface between Si particles and Sn−9Zn filler metal soldered at 300 °C with 0.1 s ultrasonic vibration: (a) Bright-field image of interface; (b−d) Electron diffraction patterns of Regions I, II and III, shown in (a), respectively

Sn and Zn, indicating the Sn–9Zn filler metal. And Fig. 3(a) shows that the oxide film was not completely removed in the interface with 0.1 s ultrasonic vibration. Interestingly, the Al–60Si alloy had large numbers of Si particles enriched at the interface, which can be seen in Figs. 3 and 5 and confirmed by Figs. 6(a, c); however, the oxide film formed on Al−60Si alloy was alumina instead of silica, which is most likely due to the stronger affinity of aluminum and oxygen than silicon and oxygen.

Figure 8 shows HRTEM images of the interface between Sn–9Zn filler metal and the Si particles. Regular crystal structures of Sn and Si could clearly be seen in Fig. 8(a), and were confirmed by the electron diffraction patterns in Figs. 8(b, c). Different local areas of the oxide film marked in Fig. 8(a) showed different structures. Most of the oxide film was identified as an amorphous layer, as shown in Fig. 8(d); some Al_2O_3 crystal structure was identified in Fig. 8(e). This observation showed that there were some Al_2O_3 crystal particles distributed in the Al_2O_3 amorphous layers.

3.2 Si particle-reinforced joints

Figure 9 shows the microstructure evolution of joints that were ultrasonically soldered for 10 s at different soldering temperatures. The typical microstructure of Al−60Si alloy (Fig. 9(c)) showed some black spherical phases (α-Al, Region 1), small black blocky phases (Si particles, Region 4), and grey rods (Zn-rich phases, Region 2) distributed in a white Sn matrix (Region 3), which confirmed by the EDS results shown in Table 5. The dissolution of Al increased with increasing the soldering temperature and α-Al phases were observed in the bond. Some Si particles without a surrounding Al matrix migrated into the bond on dissolution of Al (Figs. 9(a−d)). Similar mechanisms were revealed

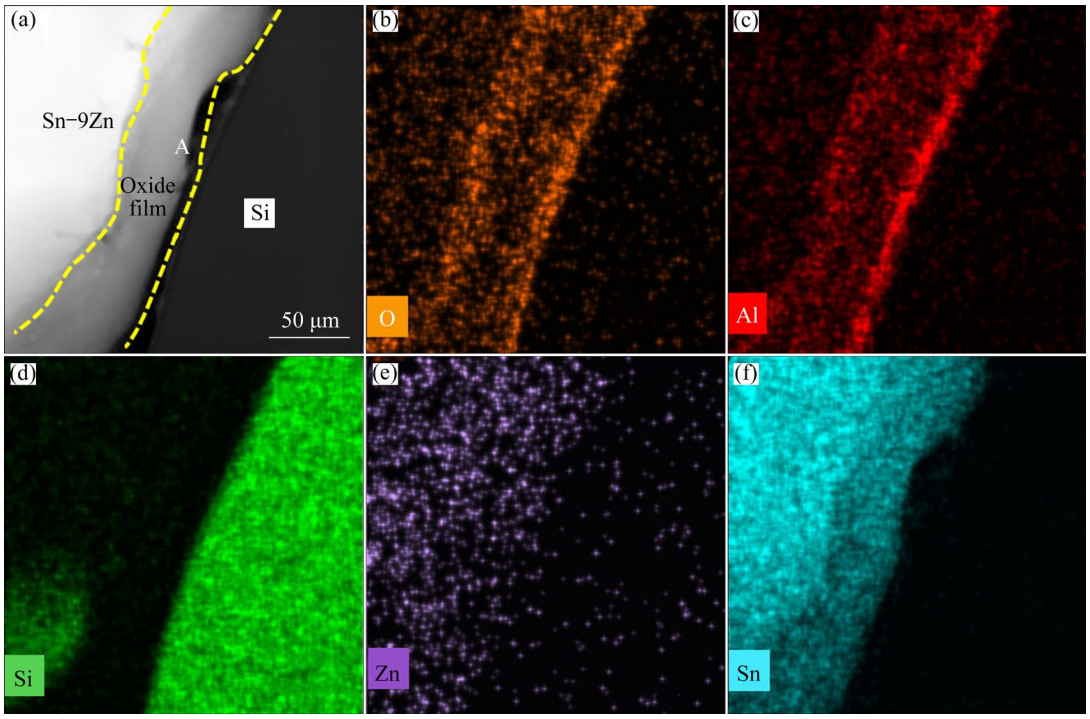

Fig. 7 Morphology (a) and element distribution mapping (b−f) of interface of Region II in Fig. 6

Table 4 Composition of Region A enclosed by yellow dashed line in Fig. 7(a) (at.%)

O	Al	Si	Sn
60.52	39.01	0.26	0.21

in the ultrasonic joining of ceramic particle-reinforced metal matrix composites [27]. It seems that the soldering temperature had little effect on the migration of Si particles into the bonds. The content of Si particles in the bond remained low, even at a soldering temperature as high as 360 °C.

The effect of ultrasonic vibration time applied on the plates was investigated and the results are shown in Fig. 10. At the soldering temperature of 330 °C, when the soldering time increased to 30 s, Si particles and α-Al spherical phases were observed in the bond (Fig. 10(a)). As the ultrasonication time increased, larger numbers of Si particles (Region 4) migrated into the bond, achieving Si particle-reinforced joints in Al−60Si alloy, as shown in Figs. 10(b, c). The compositions of the phases in the joints are shown in Table 6.

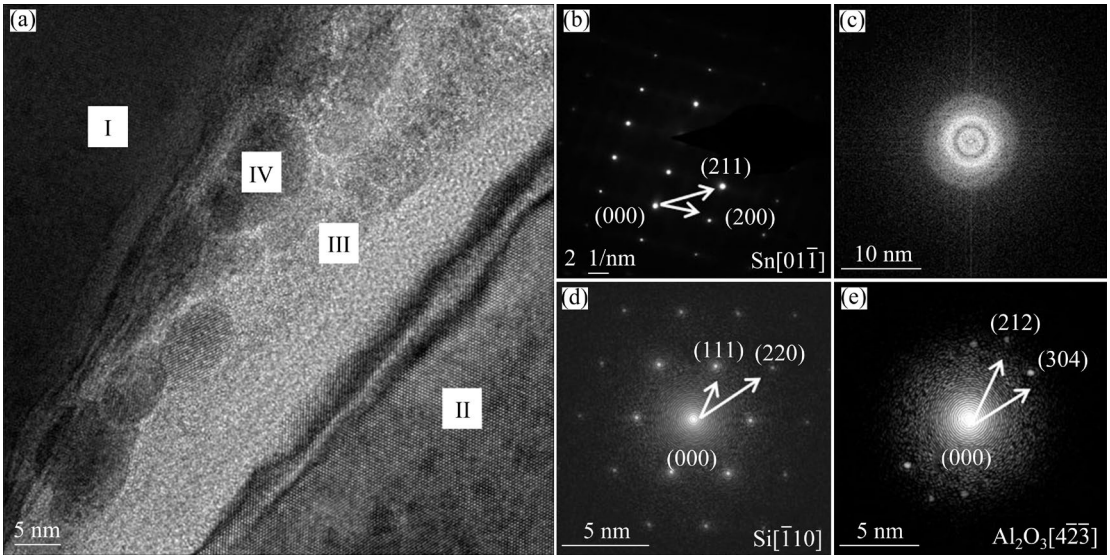

Fig. 8 High-resolution transmission electron micrograph of interface (a) and electron diffraction patterns of Regions I (b), II (c), III (d) and IV (e)

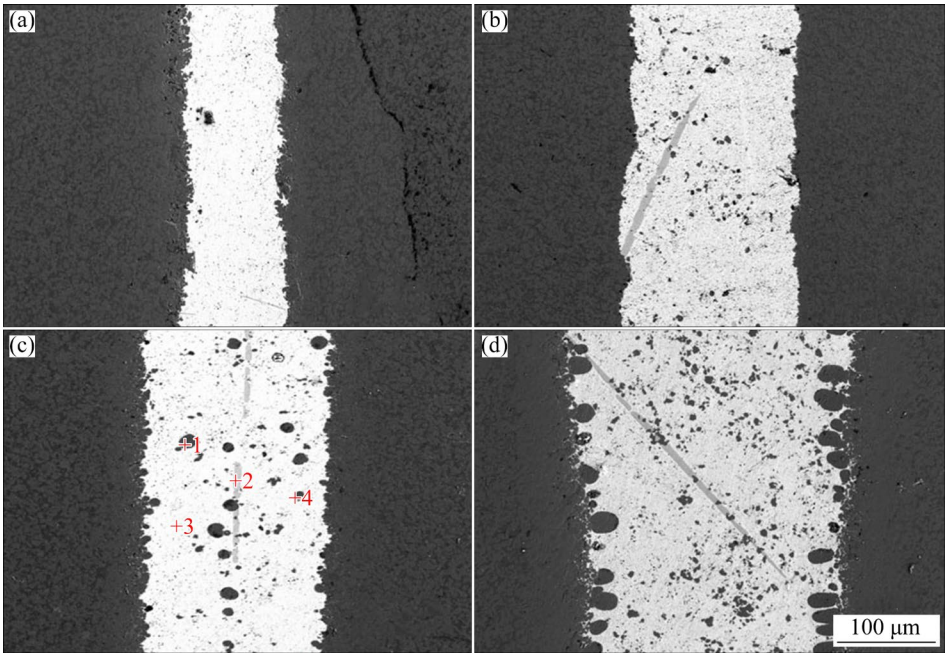

Fig. 9 Microstructures of joints ultrasonically soldered for 10 s at different temperatures: (a) 240 °C; (b) 270 °C; (c) 330 °C; (d) 360 °C

Table 5 Compositions of phases in joints in Fig. 9(c) (wt.%)

Region	Zn	Al	Si	Sn
1	8.25	90.88	0.35	0.52
2	98.19	0.95	0.41	0.45
3	1.06	0.45	0.15	98.34
4	0.33	3.16	88.72	7.79

Cavities were found in the bonds of joints soldered with excessively long ultrasonication time (Fig. 10(d)). It is shown that ultrasonic vibration time played a more important role than soldering temperature in obtaining Si particle-reinforced joints in the Al−60Si alloy.

3.3 Diffusion and dissolution at interface

The interface of joints soldered at 330 °C with 50 s ultrasonic vibration time is shown in Fig. 11(a). An amount of Si particles migrated from the Al–60Si alloy to the bond. According to the mapping scanning image (Figs. 11(b, c)), the bigger particles with round edges were Al that originated due to dissolution by Sn−9Zn solder. The smaller particles with sharper edges were identified as Si. Amounts of Si particles moved into the bond with dissolution of the Al matrix. Figures 11(d, e) show the distribution of zinc and tin, respectively, which suggests that the diffusion distance of zinc to the Al−60Si base metal was longer than that of tin. This is mainly because the solid solubility of zinc in aluminum is greater than that of tin in aluminum. The above results show that Sn−9Zn solder diffused to the Al−60Si alloy with longer ultrasonic vibration, which led to a larger amount of Al dissolution and migration of Si particles. This can be attributed to the role of ultrasound in promoting dissolution and diffusion of elements [28].

Further evidence of the promoting effect of ultrasonic vibration is shown in Fig. 12. Line scanning images show that as the ultrasonication time increased from 10 to 50 s, the diffusion distance of Sn increased from 7.1 to 35 μm, and that of zinc increased from 19 to 77 μm. The long-distance diffusion of element with increasing the ultrasonic time was mainly due to the promoting effect of ultrasound on element diffusion, which was revealed by Ref. [27]. And the diffusion distance of zinc is wider than that of tin because of larger solubility of zinc in aluminum at the soldering temperature. Thus, these results indicate that ultrasonic vibration time played an important role in promoting diffusion and dissolution of elements.

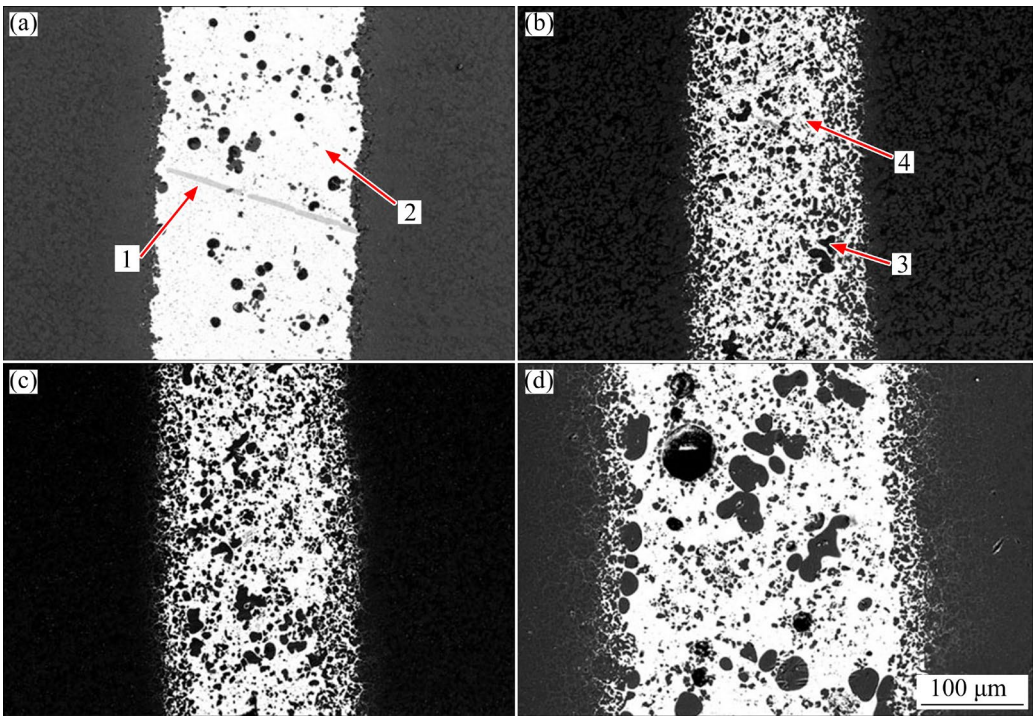

Fig. 10 Microstructures of joints soldered at 330 °C for different ultrasonication time: (a) 30 s; (b) 50 s; (c) 70 s; (d) 90 s

Table 6 Compositions of phases in joints in Fig. 10 (wt.%)

Region	Zn	Al	Si	Sn
1	98.38	1.00	0.27	0.35
2	2.07	0.35	0.25	97.33
3	10.58	88.64	0.19	0.59
4	0.32	2.46	95.03	2.19

3.4 Mechanical properties and strengthening mechanism

Figure 13 shows the shear strength of joints soldered at 330 °C with different ultrasonic vibration time. Shear strength increased with increasing ultrasonication time and peaked at 99.5 MPa when the utrasonication time was 50 s, and then declined as the ultrasonic time continued to increase. As shown in Fig. 8, the Si particles are considered to reinforce the joints, which may have a significant impact on mechanical properties. Figure 11 shows that the volume fraction of silicon particles in the joints increased with ultrasonic time, and the mechanical properties increased with the volume fraction of silicon. As the ultrasonic vibration was 50 s, the volume fraction of Si particle increased to 35.7%. However, according to Fig. 9(d), the mechanical properties of the joint with 90 s ultrasonic soldering time reduced for the defects in the bond. And volume fraction of Al increased with the increasing time of ultrasonic vibration, peaked at 20.5% as the ultrasonic time was 70 s, which was also considered to contribute to the mechanical properties of the joints. The volume fraction of Si is much higher than that of Al and positively correlated with mechanical properties, which means that Si plays the most important role in strengthening the joints.

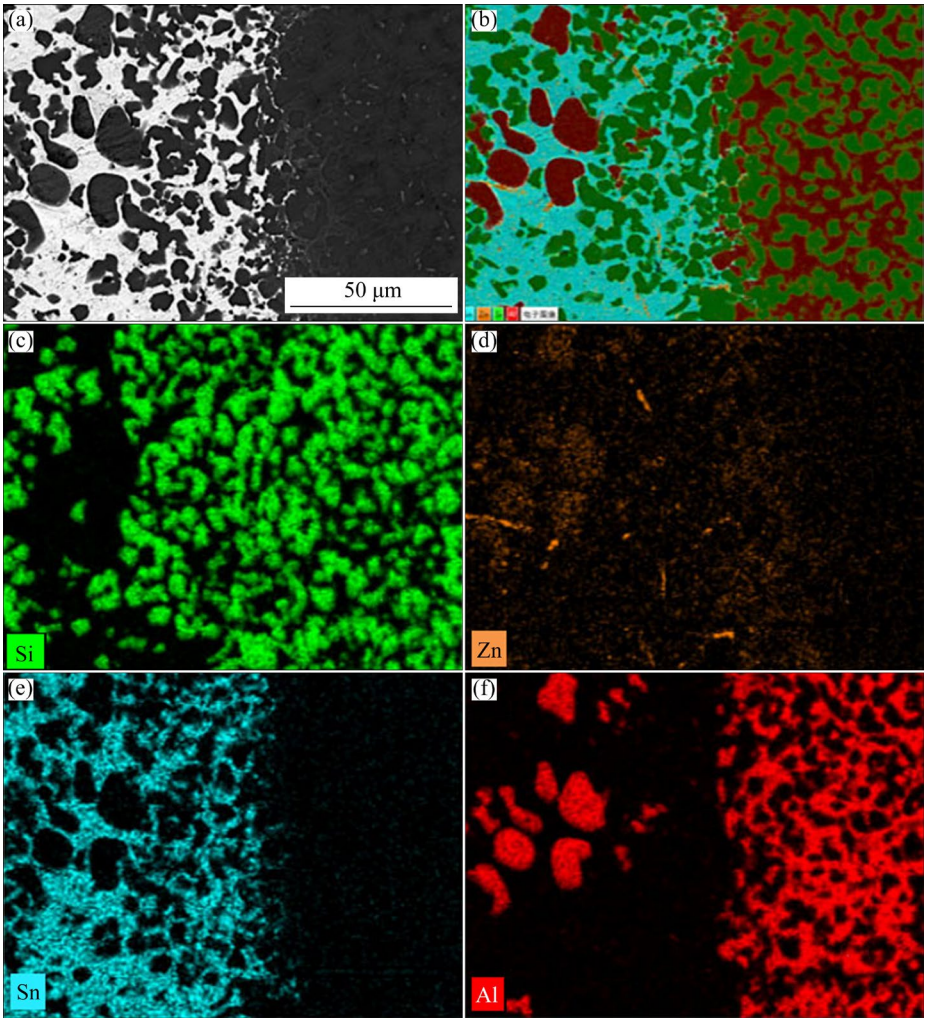

Fig. 11 Morphology of interface (a) and mapping scannings of elements (b−f) of joints soldered at 330 °C with 50 s ultrasonic vibration

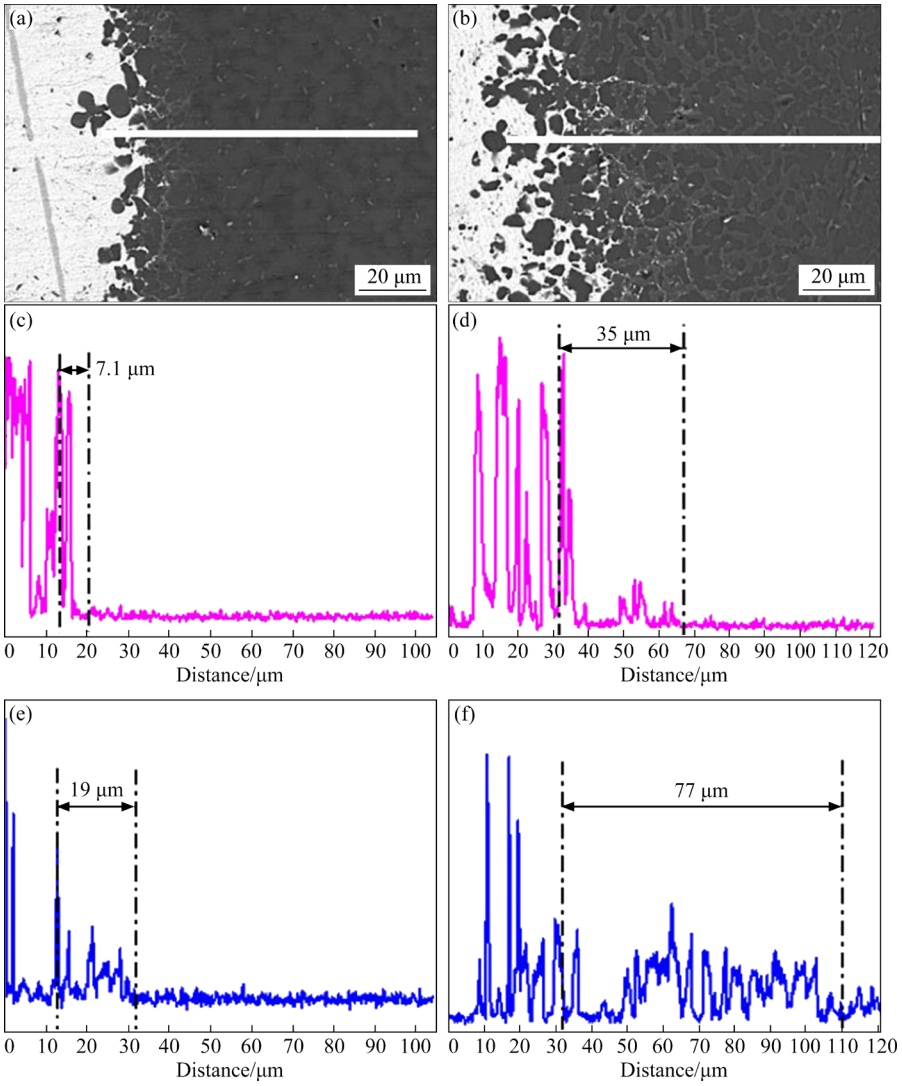

Fig. 12 Line scanning images (a, b) and distributions of elements at Sn (c, d) and Zn (e, f) interface of joints soldered at 330 °C with different ultrasonication time: (a, c, e) 10 s; (b, d, f) 50 s

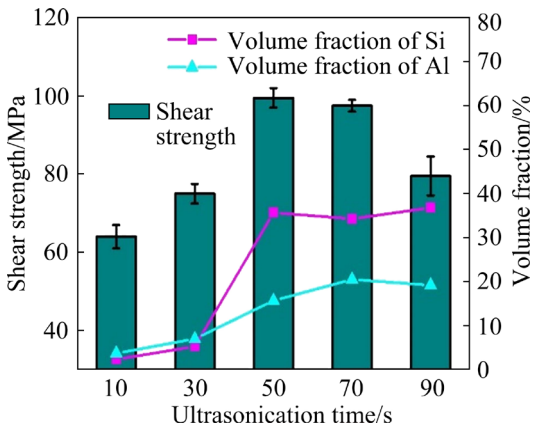

Fig. 13 Mechanical properties of joints with different ultrasonication time

Figure 14(a) shows two opposite fracture surface of joints that were ultrasonically soldered for 10 s at 330 °C. The fracture surfaces present brittle features with flat morphology. Figures 14(c, d) show that both sides of the fracture surface were rich in tin, indicating that the fracture occurred in the seam. Figures 14(e, f) show that little aluminum or silicon accumulated at the edge of the fracture surface, which means that this region was the interface. Therefore, most fracture occurred in the joint seam, suggesting that this was the weakest region of the joint.

When the ultrasonication time increased to 50 s (Fig. 15), the left side of the fracture was rich in tin and zinc, and the right side was rich in aluminum and silicon. This suggests that the left side was the Sn−9Zn solder in the seam and the other side was Al−60Si alloy base metal, and therefore fracture occurred in the interface between

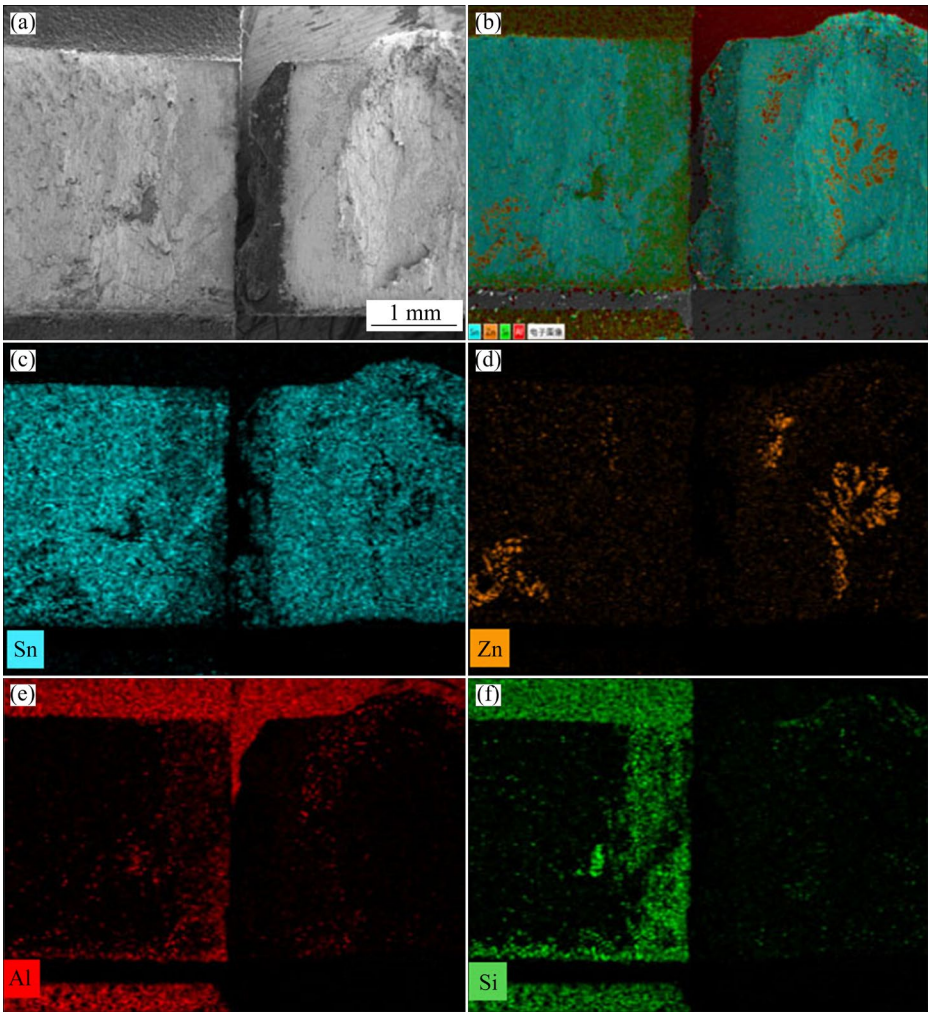

Fig. 14 Morphology of fracture surfaces (a) and distributions of elements (b−f) of joints ultrasonically soldered for 10 s

the solder and base metal. Figure 13 shows that shear strength of joints soldered for 10 s was lower than that of joints soldered for 50 s. The fracture position moved from the seam to the interface, implying that the seam was strengthened as the ultrasonic vibration time increased to 50 s. Figure 10 shows a considerable amount of Si particles distributed in the seam that was ultrasonically soldered for 50 s, while there were few Si particles in the seam that was soldered for 10 s (Fig. 9(c)). It is thus considered that Si particles reinforced the joints, leading to transition of the fracture location.

Figure 16 illustrates the formation of Si particulate reinforced joints. Figure 16(a) shows that, at the beginning of soldering, small areas of the oxide films were broken by the ultrasonic cavitation effect, and solders wetted on the oxide films. Few Si particles and Zn-rich phases could be observed in the joints. With the increasing of ultrasonic time, more and more oxide film was removed by ultrasonic vibration, and Sn−9Zn solders diffused to hypereutectic Al−60Si matrix, leading to amount of element Al to dissolve to the bond. And there were areas of dissolution zone under the oxide film with the free Si particles, as shown in Figs. 16(b) and 3(c). And then, the oxide films were totally removed by the ultrasound (Fig. 16(c)), and zinc and tin elements diffused to the base metal, leading to more and more Al dissolution. Round Al phases were observed in the center of the seam. And more and more Si particles gathered in both sides of the joint. At last, as the ultrasonic vibration continued to increase, amount of diffusion and solution occurred between solders and hypereutectic Al−60Si base mental. A large number of Si particles without Al surrounding migrated to the bond, forming a uniform particle reinforced joint under the ultrasonic disturbance, as shown in Fig. 16(d).

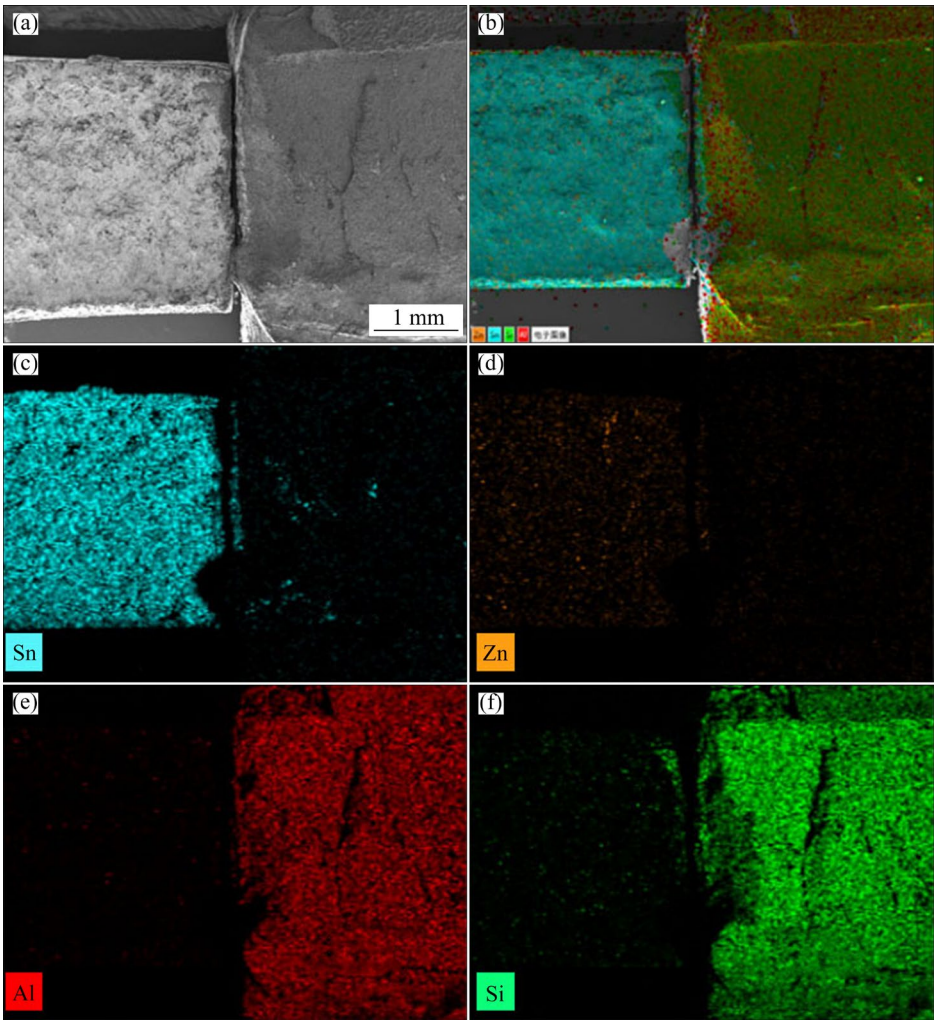

Fig. 15 Morphology of fracture surface (a) and distributions of elements (b−f) of joints ultrasonically soldered for 50 s

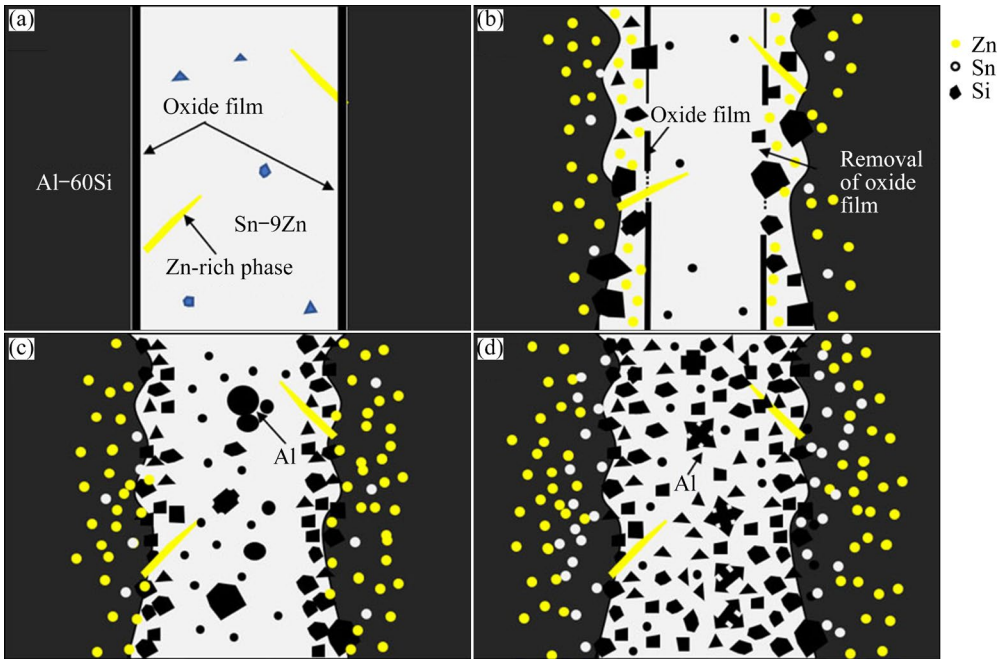

Fig. 16 Formation of Si particle reinfored joints under ultrasonic soldering of hypereutectic Al−60Si alloys: (a) At beginning of wetting; (b) Removal of oxide film; (c) Diffusion and dissolution; (d) Si particle reinforced joint

4 Conclusions

(1) The oxide film of Al−60Si alloy at the interface was identified by TEM analysis as amorphous Al_2O_3. The oxide of Si particles in the base metal was also alumina. The oxide film was observed to be removed by ultrasonic vibration.

(2) Si particle-reinforced joints (35.7 vol.%) were obtained by increasing the ultrasonication time. The maximum shear strength was 99.5 MPa for soldering at 330 °C with an ultrasonic vibration time of 50 s.

(3) A model of forming of Si particles reinforced joint under the ultrasound is proposed. Ultrasonic vibration promoted diffusion of Sn and Zn and dissolution of Al. Si particles without a surrounding Al matrix migrated to the seam.

(4) Joints with few Si particles mainly fractured in the seam. Fracture of joints with higher amount of Si particles occurred in the interface, which showed that Si particles could reinforce the joints.

CRediT authorship contribution statement

Yuan-xing LI: Conceptualization, Methodology, Writing − Original draft, Writing − Review & editing; **Xiang-bo ZHENG:** Methodology, Data curation; **Chao-zheng ZHAO:** Investigation; **Zong-tao ZHU:** Writing − Review & editing; **Yu-jie BAI:** Investigation; **Hui CHEN:** Resources.

Declaration of competing interest

The authors declare that they have no known competing financial interests or personal relationships that could have appeared to influence the work reported in this paper.

Acknowledgments

The authors appreciate financial support from the National Natural Science Foundation of China (Nos. 52275385, U2167216) and Sichuan Province Science and Technology Support Program, China (No. 2022YFG0086).

References

[1] CESCHINI L, MESSIERI S, MORRI A, SEIFEDDINE S, TOSCHI S, ZAMANI M. Effect of Cu addition on overaging behaviour, room and high temperature tensile and fatigue properties of A357 alloy [J]. Transactions of Nonferrous Metals Society of China, 2020, 30: 2861−2878. https://doi.org/10.1016/S1003-6326(20)65427-9.

[2] ZHAO Y H. In situ thermomechanical processing to avoid grain boundary precipitation and strength-ductility loss of age hardening alloys [J]. Transactions of Nonferrous Metals Society of China, 2021, 31: 1205−1216. https://doi.org/10.1016/S1003-6326(21)65572-3.

[3] KIMURA T, NAKAMOTO T, MIZUNO M, ARAKI H. Effect of silicon content on densification, mechanical and thermal properties of Al−*x*Si binary alloys fabricated using selective laser melting [J]. Materials Science and Engineering A, 2017, 682: 593−602. https://doi.org/10.1016/j.msea.2016.11.059.

[4] JIA Y D, MA P, PRASHANTH K G, WANG G, YI J, SCUDINO S, CAO F Y, SUN J F, ECKERT J. Microstructure and thermal expansion behavior of Al−50Si synthesized by selective laser melting [J]. Journal of Alloys and Compounds, 2017, 699: 548−553. https://doi.org/10.1016/j.jallcom.2016.12.429.

[5] GAN J Q, HUANG Y J, WEN C, DU J. Effect of Sr modification on microstructure and thermal conductivity of hypoeutectic Al−Si alloys [J]. Transactions of Nonferrous Metals Society of China, 2020, 30: 2879−2890. https://doi.org/10.1016/S1003-6326(20)65428-0.

[6] ZHANG W L, DING D Y, GAO P. High volume fraction Si particle-reinforced aluminium matrix composites fabricated by a filtration squeeze casting route [J]. Materials & Design, 2016, 90: 834−838. https://doi.org/10.1016/j.matdes.2015.11.033.

[7] MA Y K, WANG M X, LIU Y N, CAI B. Microstructures and corrosion behaviors of Al−6.5Si−0.45Mg−*x*Sc casting alloy [J]. Transactions of Nonferrous Metals Society of China, 2022, 32: 424−435. https://doi.org/10.1016/S1003-6326(22)65804-7.

[8] FANG J, ZHONG Y H, XIA M K, ZHANG F W. Mechanical and thermo-physical properties of rapidly solidified Al−50Si−Cu (Mg) alloys for thermal management application [J]. Transactions of Nonferrous Metals Society of China, 2021, 31: 586−594. https://doi.org/10.1016/S1003-6326(21)65521-8.

[9] LI Y, JIANG T, WEI B W, XU B Y, XU G M, WANG Z D. Microcharacterization and mechanical performance of an Al−50Si alloy prepared using the sub-rapid solidification technique [J]. Materials Letter, 2020, 263: 127287. https://doi.org/10.1016/j.matlet.2019.127287.

[10] DAI J, HUANG J, LI Z, WU Y. Microstructure and mechanical properties of high power CO_2 laser welded joint of Mg-rare earth alloy NZ30K [J]. Physics Procedia, 2010, 5: 511−516. https://doi.org/10.1016/j.phpro.2010.08.174.

[11] LIU H J, HU Y Y, ZHAO Y Q. Microstructural characteristics and formation mechanism of friction stir welds of SiC particulates reinforced Al−Si matrix composites [J]. Materials Letter, 2015, 158: 136−139. https://doi.org/10.1016/j. matlet.2015.05.158.

[12] GUO W B, LENG X S, LUAN T M, YAN J C, HE J S. Ultrasonic-promoted rapid TLP bonding of fine-grained 7034 high strength aluminum alloys [J]. Ultrasonics Sonochemistry, 2017, 36: 354−361. https://doi.org/10.1016/j.ultsonch.2016. 12.002.

[13] WANG Q, ZHU L, CHEN X G, YAN J C, XIE R S, LI P H, WANG Z H, WANG Z Q, LI Y T, ZHOU X Y. Si particulate-reinforced Zn−Al based composites joints of hypereutectic Al−50Si alloys by ultrasonic-assisted soldering [J]. Materials & Design, 2016, 107: 41−46. https://doi.org/10.1016/j.matdes. 2016.05.121.

[14] WANG H B, CHEN H S, SUN Q Z, WANG B J, YANG C.

Influence of bonding temperature on interfacial microstructure and properties of hypereutectic Al−Si joints with Cu interlayer [J]. JOM, 2021, 73: 609−619. https://doi.org/10.1007/s11837-020-04512-x.

[15] XIAO J, LI S, BAI S X, XIONG D G, TANG Y. Semisolid compression brazing of Al50Si alloy using Zn−Al−Cu filler metal assisted by SiC particles [J]. Advances in Materials Science and Engineering, 2019: 3275810. https://doi.org/10.1155/2019/3275810.

[16] LOTFI B, ROSTAMI M, SADEGHIAN Z. Effect of silicon content on microstructure of Al−Si/SiC_p composite layer cladded on A380 Al alloy by TIG welding process [J]. Transactions of Nonferrous Metals Society of China, 2014, 24: 2824−2830. https://doi.org/10.1016/S1003-6326(14)63414-2.

[17] DING Y, SHEN Z, GERLICH A P. Refill friction stir spot welding of dissimilar aluminum alloy and Al−Si coated steel [J]. Journal of Manufacturing Processes, 2017, 30: 353−360. https://doi.org/10.1016/j.jmapro.2017.10.006.

[18] XU C, LANG Q, WANG Q, CHEN Y R, YAN J C, CHEN S Y. Microstructure and mechanical properties of ultrasound-assisted soldered Al−50wt.%Si/Al−27wt.%Si joints for automotive applications [J]. JOM, 2019, 71: 2025−2032. 10.1007/s11837-019-03337-7.

[19] HASHEMABADA S G, GU Z, ANDOA T. Flux-less direct soldering of aluminum by ultrasonic surface activation [J]. Journal of Materials Processing Technology, 2016, 233: 135−141. https://doi.org/10.1016/j.jmatprotec.2016.02.015.

[20] SUN Q Z, WANG H B, YANG C. Microstructure and properties of the Al−27Si/Cu/Al−50Si joint brazed by the partial transient liquid phase bonding [J]. Metallurgical and Materials Transactions B, 2018, 49: 933−938. https://doi.org/10.1007/s11663-018-1264-1.

[21] XU L, WANG H B, SUN Q Z, WAN W C, CHEN H S. Effect of bonding temperature on microstructure and shear strength of the dissimilar Al/Al−27Si joints bonded by partial transient liquid phase bonding [J]. Journal of Manufacturing Processes, 2019, 41: 297−306. https://doi.org/10.1016/j.jmapro.2019. 04.004

[22] CUI W, WANG C W, YAN J C, WANG Z P, WEI D Q. Wetting and reaction promoted by ultrasound between sapphire and liquid Al−12Si alloy [J]. Ultrasonic Sonochemistry, 2013, 20: 196−201. 10.1016/j.ultsonch.2012.07.015.

[23] XU Z W, MA L, YAN J C, YANG S Q, DU S Y. Wetting and oxidation during ultrasonic soldering of an alumina reinforced aluminum-copper-magnesium (2024 Al) matrix composite [J]. Composites Part A: Applied Science and Manufacturing, 2012, 43: 407−414. https://doi.org/10.1016/j.compositesa.2011.12.006.

[24] XU Z W, YAN J C, ZHANG B Y, KONG X L, YANG S Q. Behaviors of oxide film at the ultrasonic aided interaction interface of Zn−Al alloy and Al_2O_{3p}/6061Al composites in air [J]. Materials Science and Engineering A, 2006, 415: 80−86. https://doi.org/10.1016/j.msea.2005.09.068.

[25] WANG Q, CHEN X G, ZHU L, YAN J C, LAI Z W, ZHAO P Z, BAO J C, LV G C, YOU C, ZHOU X Y, ZHANG J, LI Y T. Rapid ultrasound-induced transient-liquid-phase bonding of Al−50Si alloys with Zn interlayer in air for electrical packaging application [J]. Ultrasonic Sonochemistry, 2017, 34: 947−952. https://doi.org/10.1016/j.ultsonch.2016.08.004.

[26] ZHU L, WANG Q, SHI L, ZHANG X, YANG T H, YAN J C, ZHOU X Y, CHEN S Y. Ultrarapid formation of multi-phase reinforced joints of hypereutectic Al−Si alloys via an ultrasound-induced liquid phase method using Sn−51In interlayer [J]. Materials Science and Engineering A, 2018, 711: 94−98. https://doi.org/10.1016/j.msea.2017.11.014.

[27] WANG Y, LI Y X, HAN K, WAN L P, ZHANG X, JIAO S J, SHI X, JIANG C, ZHU Z T. Microstructure and mechanical properties of sol-enhanced nanostructured Ni−Al_2O_3 composite coatings and the applications in WC-Co/steel joints under ultrasound [J]. Materials Science and Engineering A, 2020, 775: 138977. https://doi.org/10.1016/j.msea. 2020.138977.

[28] WANG Y, LI Y X, SHI X, ZHENG X B, ZHU Z T, CHEN H. Direct soldering of TiO_2 nanotubes in air by ultrasonic vibration [J]. Ceramics International, 2021, 47: 19254−19259. https:// doi.org/10.1016/j.ceramint.2021.03.221.

超声辅助钎焊制备原位硅颗粒增强过共晶 Al−60Si 合金接头

李远星，郑向博，赵朝政，朱宗涛，白玉杰，陈 辉

西南交通大学 材料科学与工程学院 教育部材料先进技术重点实验室，成都 610031

摘 要：为了改善过共晶 Al−60Si 合金的润湿性，提高接头的力学性能，采用 Sn−9Zn 焊料超声焊接 Al−60Si 合金，得到了原位 Si 颗粒增强的良好接头。采用透射电镜(TEM)对 Al−60Si 合金界面处的氧化膜进行分析，鉴定其物相为非晶 Al_2O_3。并且，母材中 Si 颗粒的氧化膜经鉴定也是 Al_2O_3。经过试验发现氧化膜的去除主要是依靠超声振动，而非保温处理。通过延长超声时间，可获得硅颗粒增强接头(35.7%，体积分数)。当焊接温度为 330 ℃、超声振动时间为 50 s 时，焊缝抗剪强度最大，达到 99.5 MPa。提出了超声作用下 Si 颗粒增强接头的形成机理模型，认为超声振动起到了促进 Al 溶解和 Si 颗粒迁移的作用。

关键词：过共晶 Al−60Si 合金；超声波辅助钎焊；硅颗粒增强相；Sn–9Zn 钎料

(Edited by Bing YANG)